AIAA SciTech Forum
6-10 January 2020, Orlando, FL
AIAA Scitech 2020 Forum

10.2514/6.2020-0384

Numerical Investigation of Non-Synchronous Vibration with Fluid-Structure Interaction using Delayed Detached Eddy Simulation

Purvic Patel* and Hong-Sik Im† and Gecheng Zha‡
Dept. of Mechanical and Aerospace Engineering
University of Miami, Coral Gables, Florida 33124
E-mail: gzha@miami.edu

A Fluid-Structure Interaction (FSI) simulation is carried out for GE 1-1/2 stage high speed compressor using the Delayed Detached Eddy Simulation (DDES) based on the Spalart-Allmaras (SA) turbulence model. The structural motion equations and the unsteady spatially filtered compressible Navier-Stokes equation with the SA-DDES turbulence model are solved in a fully coupled manner. A Low Diffusion E-CUSP Riemann solver is used for the inviscid flux with a 3rd order WENO reconstructed conservative variables and a 2nd order central differencing scheme for the viscous flux. The tip vortex instability generates an excitation force with the non-engine order frequency. The predicted NSV frequency shows an excellent agreement with the rig test measurement.

I. Nomenclature

L_{ref}	=	Reference length
ρ_∞	=	Freestream density
U_∞	=	Freestream velocity
μ_∞	=	Freestream dynamics viscosity
Ω	=	Vorticity / Rotational speed of a rotor
Re	=	Reynolds number
R_o	=	Rossby number
$i,\ j,\ k$	=	Dummy indices for Indicial / Einstein summation notation
κ	=	von-Karman constant
$u,\ v,\ w$	=	Cartesian velocity components in $x,\ y$ and z direction respectively
$\mathbf{l},\ \mathbf{m},\ \mathbf{n}$	=	Elemental surface normal vector in ξ, η and ζ directions
$U,\ V,\ W$	=	Contravariant velocities in ξ, η and ζ directions
P_ν	=	Production of turbulence viscosity
D_ν	=	Destruction of turbulence viscosity
T_ν	=	Trip term for turbulence viscosity
Δq	=	Difference between the velocity at the field point and that at the trip (on the wall)
Δx_t	=	Grid spacing along the wall at the trip
ω_t	=	Wall vorticity at the trip
d_w	=	Distance from the nearest wall gridpoint
d_t	=	Distance from the field point to the trip
SA-noft2	=	Spalart-Allmaras One-Equation Model without f_{t2} Term
LES	=	Large Eddy Simulation
DES	=	Detached-Eddy Simulation
DDES	=	Delayed Detached-Eddy Simulation
NSV	=	Non-Synchronous Vibration
SFV	=	Separated Flow Vibration

*Ph.D. Candidate
†Ph.D., Currently working at Doosan ATS America
‡Professor, ASME Fellow, AIAA associate Fellow.

WENO = Weighted Essentially Non-Oscillatory
CUSP = Convective Upwind and Splitting Pressure

II. Introduction

An understanding of the fluid-structure interaction is vital in an industry with the pronounced vibration as it can lead to a catastrophic failure of the structure. A vibration can be broadly classified as a forced or self-excited vibration. In the case of turbomachinery, the forced-excitation of rotor blades arises from aerodynamic excitations such as inlet flow distortion, upstream wakes, etc. Almost all sources, except those from the rotating stall, must be at harmonics of the rotational frequency of the rotor itself [1]. In a self-excited vibration, the rotor blades are vibrating at a natural frequency due to insufficient mechanical and aerodynamic damping to overcome the vibrations generated by the gas stream. In the last two decades with a lean rotor blade design, researches have observed another self-excited Non-Synchronous Vibration (NSV).

In a non-synchronous vibration, occurring in the stable operating range of a compressor, the frequency response is not necessarily the blade natural frequency [2]. In this non-engine order excitation, a large amplitude vibration occurs due to the complex flow phenomenon such as rotating instability (RI) [2–9] in the tip region. Experimental investigations by Baumgartner et al. [3] and Mailach et al. [4] have found that the rotating instabilities in the tip region lead to the NSV under certain operating conditions. Based on the experimental and numerical analysis on a low-speed single-stage fan with outlet guide vanes at high load-operating point, März et al. [5] have observed the NSV of roughly half the Blade Passing Frequency (BPF) due to the tip flow instability. According to the jet core feedback theory proposed by Thomassin et al. [10], the NSV is caused by the resonance jet condition — the wavelength of acoustic reflection matching with the jet-to-plate distance. This creates a significant amplification of the pressure unsteadiness on the plate. Thomassin et al. [6] validated their theory with a high-pressure compressor first stage rotor and deswirl vanes, and good agreement between the resonance condition criterion and experimental data is observed. Recent experimental work by Brandstetter et al. [11] suggests the formation and propagation of Radial Vortex (RV) induces the NSV.

An Unsteady Reynolds-Averaged Navier-Stokes (URANS) solver is overly diffusive as it models all the scales of eddies. Therefore it fails to provide the flow details like the Large Eddy Simulation (LES) model. Owing to the modeling of eddies with the different length scales, URANS does not resolve the large energy-containing eddies. Its effect can be seen on the under-predicted Reynolds shear stresses in the separated region and thereby increased flow separation.

In LES, filtered, time-dependent Navier-Stokes equations are solved. Large energy-containing eddies are resolved whereas the effect of small scale isotropic eddies is modeled. This strategy permits to reveal more flow features at the cost of large computational resources to resolve the boundary layer. Therefore, it is not widely used for high Reynolds number industry applications [12, 13].

An alternative is to use the RANS / LES Hybrid turbulence model which takes the advantages of URANS's high efficiency and LES's high accuracy. In 1997, Spalart et al. [12] proposed the Detached-Eddy Simulation (DES), commonly referred to as DES97, based on the one-equation Spalart-Allmaras (SA) turbulence model. The goal of this model is to simulate the boundary layer in the RANS mode and switch to the LES mode away from the wall or highly separated flow region [14]. As the mode switch is an explicit function of local grid size, it imposes the rigorous meshing guidelines to avoid the Grid-Induced Separation (GIS) and the Modeled-Stress Depletion (MSD). To circumvent these problems with the ambiguous grids, Spalart et al. [15] introduces a blending function similar to the one introduced by Menter et al. [16]. This blending function essentially shields the boundary layer under rigorous mesh refinement and delays the unwarranted switch to the LES mode. This newer version is termed as Delayed Detached-Eddy Simulation (DDES). In the past, most of the NSV simulations of an axial-compressor are performed using a URANS [2, 8, 17–20] and few literatures show an application of a hybrid turbulence model [9, 21, 22].

Fig. 1 shows a strain gauge response of GE 1-1/2 high-speed compressor first stage rotor blade NSV [2]. Here, rotor blades have a tip clearance of 1.1 % tip axial chord. A step-change in the NSV frequency is observed in the rig test with the variation of the rotational speed of the compressor. The Separated Flow Vibration frequency along with the amplitude is also shown at various rotor speeds. Based on the numerical investigation of the rigid blades by Kielb et al. [2], using the URANS model on the 1/7th annulus sector of a compressor row, the NSV is caused by the vortex unsteadiness on the suction side near 75 % and the tip flow oscillation near the leading edge. Their predicted frequency is approximately 9 % lower than the rig test. Im et al. [8] carried out a similar investigation with rigid blades using URANS and their predicted NSV frequency is 3.3 % lower than the rig test result. Im et al. [9] carried out further investigation using the Delayed DES hybrid turbulence model considering rigid blades to better understand the NSV mechanism. With the hybrid turbulence model, the NSV frequency is under-predicted by 14.7 %. Based on their results,

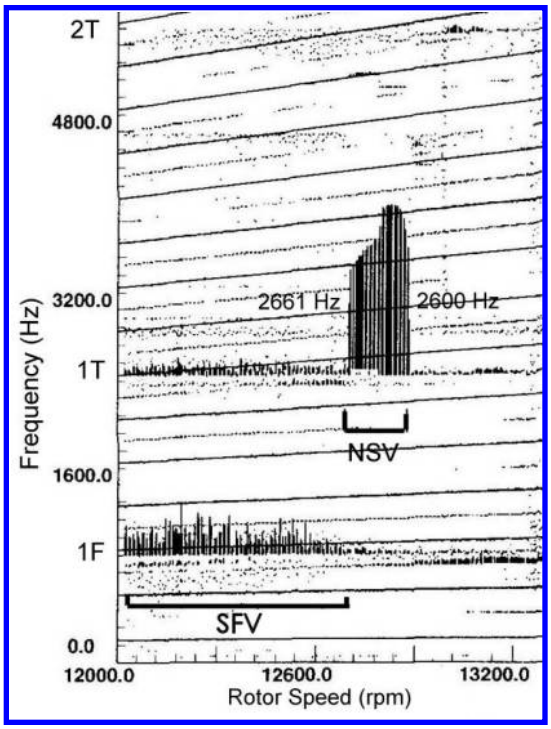

Figure 1 Strain gauge response of first stage rotor blades in a rig test [2]

this under-prediction is attributed to the tendency of DDES to predict rotor stall earlier than the URANS and the NSV can be achieved only at the higher mass flow rate, which generates a lower frequency [9]. Patel et al. [22] investigated the compressor NSV problem with rigid blades case using the Scale Adaptive Simulation hybrid turbulence model and their numerical results show 2.96 % under-prediction, which is an improvement over the URANS turbulence model [23] results.

In the present study, NSV mechanism is investigated with the Fluid-Structure Interaction with vibrating blades using the SA-DDES. A system of five decoupled model equations is solved in a fully coupled manner with the flow solver. A tip-flow instability observed as the driver for the NSV. The predicted NSV frequency agrees well with the experiment.

III. Governing Equations

The spatially filtered, unsteady compressible Navier-Stokes equations along with the SA based DDES turbulence model are solved in fully coupled manner using an implicit unfactored Gauss-Seidel line iteration to achieve high convergence rate. These equations are nondimensionalized using L_{ref}, ρ_∞, U_∞ and μ_∞ and the governing equations in generalized coordinates are written as:

$$\frac{\partial Q}{\partial t} + \frac{\partial E}{\partial \xi} + \frac{\partial F}{\partial \eta} + \frac{\partial G}{\partial \zeta} = \frac{1}{Re}\left[\frac{\partial R}{\partial \xi} + \frac{\partial S}{\partial \eta} + \frac{\partial T}{\partial \zeta}\right] + S_v \tag{1}$$

where,

$$
Q = \frac{1}{J}\begin{bmatrix} \rho \\ \rho u \\ \rho v \\ \rho w \\ \rho e \\ \rho\tilde{\nu} \end{bmatrix}, \quad E = \begin{bmatrix} \rho U \\ \rho u U + p l_x \\ \rho v U + p l_y \\ \rho w U + p l_z \\ (\rho e + p)U - p l_t \\ \rho\tilde{\nu} U \end{bmatrix}, \quad F = \begin{bmatrix} \rho V \\ \rho u V + p m_x \\ \rho v V + p m_y \\ \rho w V + p m_z \\ (\rho e + p)V - p m_t \\ \rho\tilde{\nu} V \end{bmatrix}
$$

$$
G = \begin{bmatrix} \rho W \\ \rho u W + p n_x \\ \rho v W + p n_y \\ \rho w W + p n_z \\ (\rho e + p)W - p n_t \\ \rho\tilde{\nu} W \end{bmatrix}, \quad R = \begin{bmatrix} 0 \\ \tau_{xi} l_i \\ \tau_{yi} l_i \\ \tau_{zi} l_i \\ (u_j \tau_{ij} - q_i) l_i \\ \frac{\rho}{\sigma}(\nu + \tilde{\nu}) \frac{\partial \tilde{\nu}}{\partial x_i} l_i \end{bmatrix}, \quad S = \begin{bmatrix} 0 \\ \tau_{xi} m_i \\ \tau_{yi} m_i \\ \tau_{zi} m_i \\ (u_j \tau_{ij} - q_i) m_i \\ \frac{\rho}{\sigma}(\nu + \tilde{\nu}) \frac{\partial \tilde{\nu}}{\partial x_i} m_i \end{bmatrix} \tag{2}
$$

$$
T = \begin{bmatrix} 0 \\ \tau_{xi} n_i \\ \tau_{yi} n_i \\ \tau_{zi} n_i \\ (u_j \tau_{ij} - q_i) n_i \\ \frac{\rho}{\sigma}(\nu + \tilde{\nu}) \frac{\partial \tilde{\nu}}{\partial x_i} n_i \end{bmatrix}, \quad S_v = \frac{1}{J}\begin{bmatrix} 0 \\ 0 \\ \rho R_o^2 y + 2\rho R_o w \\ \rho R_o^2 z - 2\rho R_o v \\ 0 \\ P_\nu - D_\nu + T_\nu + \frac{1}{Re}\frac{\rho}{\sigma} c_{b2} \frac{\partial \tilde{\nu}}{\partial x_i}\frac{\partial \tilde{\nu}}{\partial x_i} \end{bmatrix}
$$

where, Q is the conservative variable vector. The flux vectors E, F and G represent the inviscid flux through the cell interface with the normal in positive ξ, η and ζ directions respectively. The viscous term vectors R, S, and T are represented in indicial notations, using dummy indices i and j, in Eq. (2). The source term vector, S_v, per unit volume represents the source contribution in momentum equations depending on the reference frame for turbomachinery and the SA-DDES turbulence model source.

l_t, m_t, n_t are the components of the interface contravariant velocity of the control volume in ξ, η, ζ directions respectively. $\mathbf{l}$, $\mathbf{m}$, $\mathbf{n}$ represent the normal vectors with their magnitudes equal to the elemental surface areas and pointing in the increasing ξ, η, ζ directions, respectively. J is the Jacobian of the coordinate transformation. Contravariant variant velocities (Eq. (4)) through the each cell interface are defined as:

$$
\begin{aligned}
\mathbf{l} = \frac{\nabla\xi}{J},\ \mathbf{m} = \frac{\nabla\eta}{J},\ \mathbf{n} = \frac{\nabla\zeta}{J} \\
l_t = \frac{\xi_t}{J},\ m_t = \frac{\eta_t}{J},\ n_t = \frac{\zeta_t}{J}
\end{aligned} \tag{3}
$$

$$
\begin{aligned}
U &= l_t + l_i V_i = l_t + l_x u + l_y v + l_z w \\
V &= m_t + m_i V_i = m_t + m_x u + m_y v + m_z w \\
W &= n_t + n_i V_i = n_t + n_x u + n_y v + n_z w
\end{aligned} \tag{4}
$$

The relation between the total internal energy (e) and the static pressure is written as:

$$
\rho e = \frac{p}{(\gamma - 1)} + \frac{1}{2}\rho(u^2 + v^2 + w^2 - r^2 R_o^2) \tag{5}
$$

where, radius ($r = \sqrt{y^2 + z^2}$) is from the rotational x-axis.
The shear stress (τ_{ij}) and total heat flux (q_i) are given by:

$$
\begin{aligned}
\tau_{ij} &= \tau_{ij}^{lam} + \tau_{ij}^{turb} = (\mu + \mu_{DDES})\left(\frac{\partial u_i}{\partial x_j} + \frac{\partial u_j}{\partial x_i} - \frac{2}{3}\delta_{ij}\frac{\partial u_k}{\partial x_k}\right) \\
q_i &= \frac{1}{M_\infty^2}\frac{1}{\gamma - 1}\left(\frac{\mu}{Pr} + \frac{\mu_{DDES}}{Pr_t}\right)\frac{\partial T}{\partial x_i}
\end{aligned} \tag{6}
$$

where the turbulent viscosity (μ_{DDES}) is determined by the SA-DDES turbulence model. The molecular viscosity (μ) is calculated using Sutherland's law. The turbulence model source term consists of production (P_ν), destruction (D_ν), trip (T_ν) and diffusion terms which are defined as:

$$\begin{aligned} P_\nu &= \rho c_{b1}\,(1 - f_{t2})\,\hat{S}\tilde{\nu} \\ D_\nu &= \frac{1}{Re}\left[\rho\left(c_{w1} f_w - \frac{c_{b1}}{\kappa^2} f_{t2}\right)\left(\frac{\tilde{\nu}}{d_w}\right)^2\right] \\ T_\nu &= Re\left[\rho f_{t1}\,(\Delta q)^2\right] \end{aligned} \tag{7}$$

Auxiliary relations:

$$\begin{aligned} &\mu_{DDES} = \rho\tilde{\nu} f_{v1}\,, && \chi = \frac{\tilde{\nu}}{\nu}\,, && f_{v1} = \frac{\chi^3}{\chi^3 + c_{v1}^3} \\ &\hat{S} = \Omega + \overline{S}\,, && f_{v2} = 1 - \frac{\chi}{1 + \chi f_{v1}}\,, && f_w = g\left(\frac{1 + c_{w3}^6}{g^6 + c_{w3}^6}\right)^{1/6} \\ &g = r + c_{w2}(r^6 - r)\,, && r = min\left(\frac{\tilde{\nu}}{\hat{S}\kappa^2 d_w^2}, 10\right)\,, && f_{t2} = c_{t3}\exp\left(-c_{t4}\chi^2\right) \\ &f_{t1} = c_{t1} g_t \exp\left[-c_{t2}\frac{\omega_t^2}{\Delta U^2}\left(d_w^2 + g_t^2 d_t^2\right)\right]\,, && g_t = min\left(0.1, \frac{\Delta q}{\omega_t \Delta x_t}\right)\,, && \overline{S} = \frac{1}{Re}\frac{\tilde{\nu}}{\kappa^2 d_w^2} f_{v2} \end{aligned} \tag{8}$$

Closure coefficients in Eqs. (2), (7) and (8) are:

$$\begin{aligned} &c_{b1} = 0.1355\,, && \sigma = \frac{2}{3}\,, && c_{b2} = 0.622\,, && \kappa = 0.41 \\ &c_{w2} = 0.3\,, && c_{w3} = 2\,, && c_{v1} = 7.1\,, && c_{t3} = 1.1 \\ &c_{t4} = 2.0\,, && c_{w1} = \frac{c_{b1}}{\kappa^2} + \frac{(1 + c_{b2})}{\sigma}\,, && c_{t1} = 1.0\,, && c_{t2} = 2.0 \end{aligned} \tag{9}$$

In this study, the numerical calculation is carried out using the DDES hybrid turbulence model considering the fully turbulent flow and therefore trip term T_ν and f_{t2} are considered zero.

A. Modification for SA turbulence model [24, 25]

In order to avoid numerical difficulties arising from zero or negative $\hat{S}$, the modification, as in Eq. (11), is applied in the present study to the P_ν of SA turbulence model source term.

$$\overline{S} = \frac{1}{Re}\frac{\tilde{\nu}}{\kappa^2 d_w^2} f_{v2} \tag{10}$$

$$\hat{S} = \begin{cases} \Omega + \overline{S} & : \overline{S} \geq -c_2\Omega \\ \Omega + \frac{\Omega(c_2^2\Omega + c_3\overline{S})}{(c_3 - 2c_2)\Omega - \overline{S}} & : \overline{S} < -c_2\Omega \end{cases} \tag{11}$$

where, $c_2 = 0.7$, $c_3 = 0.9$ and set $r = 10$ if $\hat{S} = 0$.

B. Distance scale modification for DDES turbulence model

In the DES97 turbulence model, it functions as RANS in the near wall boundary layer and as a large-eddy simulation away from the wall or in the highly separated regions. This behavior in the SA turbulence model is achieved by redefining the distance scale d_w as:

$$\tilde{d} = \min\left(d_w, C_{DES}\Delta_{max}\right) \tag{12}$$

where, $C_{DES} = 0.65$ is a constant and $\Delta_{max} = \max\left(\Delta_x, \Delta_y, \Delta_z\right)$

It can be seen from Eq. (12) that the distance scale depends explicitly on the local grid size to achieve the LES behavior. This explicit function has lead to the MSD and GIS problem under the ambiguous grid. To tackle these

problems, Spalart et al. [15] proposed the DDES model, based on Menter et al. [16] to shield the boundary layer and thereby delay the LES mode. This shielding is achieved based on the eddy viscosity and the velocity gradient. The length scale in the DDES is given by:

$$\tilde{d} = d_w - f_d \max(0, d_w - C_{DES}\Delta_{max}) \tag{13}$$

where,

$$\begin{aligned} f_d &= 1 - \tanh([8r_d]^3) \\ r_d &= \frac{\nu_t + \nu}{\sqrt{U_{i,j}U_{i,j}}\kappa^2 d_w^2 Re} \end{aligned} \tag{14}$$

$U_{i,j}$ represents the velocity gradient and κ is the von Karmann constant. In the boundary layer, f_d is designed to be 0 to achieve the RANS solution and it assumes value of 1 in the LES region.

IV. Time Marching Scheme

A time-dependent control volume integrated Navier-Stokes equation can be written in the semi-discrete form as:

$$\frac{\partial Q}{\partial t} = -\frac{1}{\Delta V}\oint_S R_F.ds + S_v \tag{15}$$

where R_F is the net flux of Navier-Stokes equations discretized in space and S_v is the contribution of the source term.

Following Jameson's dual time stepping method [26], a pseudo temporal term $\partial Q/\partial\tau$ is added to the left-hand side of Eq. (15). The term $\partial Q/\partial t$ is discretized using the second-order three-point backward differencing scheme on the physical time steps $n+1$, n and $n-1$. The pseudo temporal term is discretized on two pseudo time steps (i.e. $m+1$ and m) on the same physical time step $n+1$. The final formulation of this dual time stepping method is given by:

$$\left[\left(\frac{1}{\Delta\tau} + \frac{1.5}{\Delta t}\right)I - \left(\frac{\partial RHS}{\partial Q}\right)^{n+1,m}\right]\Delta Q^{n+1,m+1} = RHS^{n+1,m} - \frac{3Q^{n+1,m} - 4Q^n + Q^{n-1}}{2\Delta t} \tag{16}$$

where,

$$RHS = -\frac{1}{\Delta V}\oint_S R_F.ds + S_v \tag{17}$$

In each physical time step, the solution is converged when $\Delta Q^{n+1,m+1} \to 0$ and therefore it has no influence on the solution accuracy.

V. Structural Model

In the rotating frame, only the vibration characteristics of the blades are dominant considering the rotor disk stiffness is much higher than blades. Therefore, blade vibration is only considered.

A. Modal Approach

The equation of motion for damped N-DOF (degree of freedom) system with the aerodynamic excitation force can be represented in matrix as:

$$[M]\{\ddot{X}\} + [C]\{\dot{X}\} + [K]\{X\} = \{F\} \tag{18}$$

where, M, C and K are the mass, damping and stiffness matrices. The total aerodynamic force (F) acting on the blade surface is defined as:

$$F = -\oint p.\hat{n}dA + \oint \tau_w.\hat{t}dA \tag{19}$$

where, $\hat{n}$ and $\hat{t}$ are the unit vector normal and tangential to the blade surface, respectively. p is the fluid static pressure and τ_w is the fluid wall shear stress acting on the blade surface.

The equations of motion for the damped system, Eq. (18), are decoupled using the mass normalized mode shape ($\tilde{\phi}$) defined as the normal modes divided by square root of the generalized mass ($\sqrt{\phi^T m\phi}$). Let $\{X\} = [\tilde{\Phi}]\{q\}$ and premultiplication of Eq. (18) by transpose $[\tilde{\Phi}]^T$ leads to

$$[\tilde{\Phi}]^T [M] [\tilde{\Phi}] \{\ddot{q}\} + [\tilde{\Phi}]^T [C] [\tilde{\Phi}] \{\dot{q}\} + [\tilde{\Phi}]^T [K] [\tilde{\Phi}] \{q\} = [\tilde{\Phi}]^T \{F\} \tag{20}$$

where, $\{q\}$ is the principal coordinates vector and $[\tilde{\Phi}] = [\tilde{\phi}_1, \tilde{\phi}_2, \ldots, \tilde{\phi}_N]^T$ with N total number of modal coordinates. Using the orthogonality of the system matrices and assuming damping matrix as a linear combination of the mass and stiffness matrices, Eq. (20) is decoupled and the i^{th} equation will have the form as:

$$\ddot{q}_i + 2\zeta_i \omega_i \dot{q}_i + \omega_i^2 q_i = \frac{\tilde{\phi}_i^T}{m_i} F \tag{21}$$

where, ω_i and ζ_i are the natural frequency and the modal damping ratio for mode i. Since the structural damping of the blade is usually very small [27], ζ of 0.001 is used for all modes in the present study. m_i denotes the i^{th} diagonal element of modal mass matrix which will be unity. In the current study, the structural system is reduced to first five mode shapes, since a few bending and torsional frequencies are usually sufficient to determine the flutter. The normalized modal equation can be given by:

$$\ddot{q}_i + 2\zeta_i \left(\frac{\omega_i}{\omega_\alpha}\right) \dot{q}_i + \left(\frac{\omega_i}{\omega_\alpha}\right)^2 q_i = \frac{\tilde{\phi}_i^{*T}}{m_i^*} . F^* . V_f^2 . \frac{b_s^2 L_{ref}}{\bar{V}} . \bar{m} \tag{22}$$

where, the dimensionless quantities are denoted by an asterisk. $V_f \left(= \frac{U}{b_s \omega_\alpha \sqrt{\bar{\mu}}}\right)$ is the flutter speed index which is an input flutter control parameter. $\bar{m}$ is the measure of blade mass, $\bar{V}$ represents the conical frustum volume and b_s is the stream-wise root semi chord. ω_α is the first torsional mode frequency in rad/s. $\bar{\mu} = \frac{\bar{m}}{\bar{V}\rho_\infty}$ is the mass ratio, i.e. the ratio between the structural mass and the mass of the equivalent volume of fluid at reference density. It is noticed that m_i^* should be equal to one when the mass normalized mode shapes are used.

The structure equations are then transformed to a state form as follows:

$$[M] \frac{\partial S}{\partial t} + [K][S] = q \tag{23}$$

where,

$$S = \begin{pmatrix} q_i \\ \dot{q}_i \end{pmatrix}, M = [I], K = \begin{pmatrix} 0 & -1 \\ \left(\frac{\omega_i}{\omega_\alpha}\right)^2 & 2\zeta_i \left(\frac{\omega_i}{\omega_\alpha}\right) \end{pmatrix}$$

$$q = \begin{pmatrix} 0 \\ \phi_i^* . F^* . V_f . \frac{b_s^2 L}{\bar{V}} . \bar{m} \end{pmatrix}$$

B. Implicit Structural Solver

To solve the structural equations with the CFD solver in a fully coupled manner [28], the decoupled structural equations are integrated using the same method as the flow governing within each physical time step as:

$$\left[\left(\frac{1}{\Delta\tau} I + \frac{1.5}{\Delta t} M + K\right)\right] \delta S^{n+1,m+1} = q^{n+1,m+1} - M \frac{3S^{n+1,m} - 4S^n + S^{n-1}}{2\Delta t} + K S^{n+1,m} \tag{24}$$

In each physical time step, flow and structural equations are solved iteratively via every successive pseudo time step until the prescribed convergence criteria is satisfied for both solver. After the convergence criteria is reached, the fluid-structural interaction proceeds to the next physical time step.

VI. Computational Set-Up

A. Geometry and mesh description

The high-speed compressor consists of 56 IGV blades, 35 Rotor blades and 70 stator blades. The tip clearance of rotor blade is 1.1 % of tip axial chord. In the present study, only 1/7th sector of full annulus is considered with 5 Nodal Diameters (NDs). To ensure high orthogonality of grid near the wall, O-mesh topology is used around a blade. The

interface block at the frame change is meshed with H-mesh topology and one-to-one connected. This ensures the flux conservation between the different reference frames. The tip region is fully gridded with 21 grid points. The mesh overview is depicted in Fig. 2. An overview of number of grid points is provided in Table 1 with the direction around the blade (i), blade to blade (j) and spanwise (k), respectively for all blades. The total mesh size of the computational domain used here is 11,886,560. The mesh refinement study is not considered, as this mesh is used earlier for the NSV study by Im et al. [9, 23].

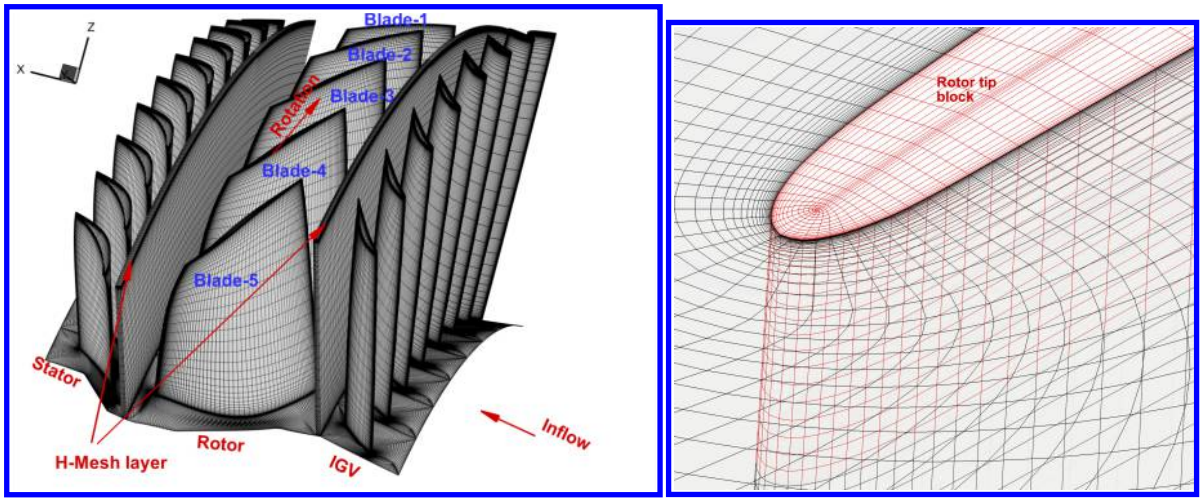

(a) 1/7th Annulus mesh **(b) Rotor tip block mesh**

Figure 2 Mesh overview[9]

Table 1 Grid points around a blade

Domain	$i \times j \times k$
Rotor blade	$201 \times 51 \times 71$
IGV	$121 \times 51 \times 71$
Stator vane	$121 \times 51 \times 71$

B. Boundary Conditions (BCs)

At the IGV inlet, the radial distributions of total pressure, total temperature, swirl angle and pitch angle is defined. A velocity component is extracted from the inner domain to determine the rest of flow variables. At the stator outlet, the radial profile of static pressure is defined. As the flow at the outlet of stator is subsonic, the rest of flow variables are extracted from the inner domain. The time shifted phase-lag boundary condition [29] is applied with five nodal diameters on the periodic boundaries. For the rotating walls, the wall static pressure for the inviscid momentum equation is determined by solving the radial equilibrium and the static pressure gradient is set to zero for the stationary walls. On the blade surface, no-slip wall boundary condition is used, whereas the remaining walls are modeled with an efficient wall boundary condition [30], which switches from no-slip wall BC to wall function if y^+ is between 11 to 300. A zero heat flux though the wall is imposed by an adiabatic equation. On the rotor and stator interface, a fully conservative sliding boundary condition is utilized [8, 31] with the mesh one-to-one connected as shown in the Fig. 2. The compressor is operating at the off-design speed of 12,880 RPM.

C. Numerical methods

The Low Diffusion E-CUSP (LDE) scheme as an accurate shock capturing Riemann solver is used for the inviscid flux. The conservative variables are reconstructed using a third order WENO scheme for it. A second order central

differencing scheme is used for the viscous flux. The implicit dual time stepping scheme after [26] is used for the temporal terms in both solvers. In each physical time step, the residual is allowed to reduce by two orders of magnitude, which is usually achieved within 30 to 35 pseudo time step iterations. A non-dimensional time step of about 0.005 is used. A structural damping ratio of 0.001 is used with zero initial structural velocity. The unsteady simulation with the DDES turbulence model is started from the converged steady state results and carried out for total of 13 revolutions. The high-scalability parallel computing is used to save the wall clock time [32]. The unsteady pressure on the blade surface causes blades to vibrate and therefore an advanced blade deforming mesh technique [33] is employed to preserve a high-quality mesh.

D. Numerical Probes

In Fig. 3, the intersection of two lines represents one numerical probe location. There are 15 numerical probes installed on the suction surface of a rotor blade and similarly on the pressure surface. Each probe location for a blade is uniquely identified by four digits and an alphabet. First two numerals describe spanwise location, remaining two digits represent its axial location in terms of percentage chord length from the leading edge and an alphabet describes suction (S) or pressure (P) side. A total number of 30 probes capture the instantaneous static pressure over a blade surface. The pressure side numerical probes are not shown in the figure however their locations are identical to the suction surface.

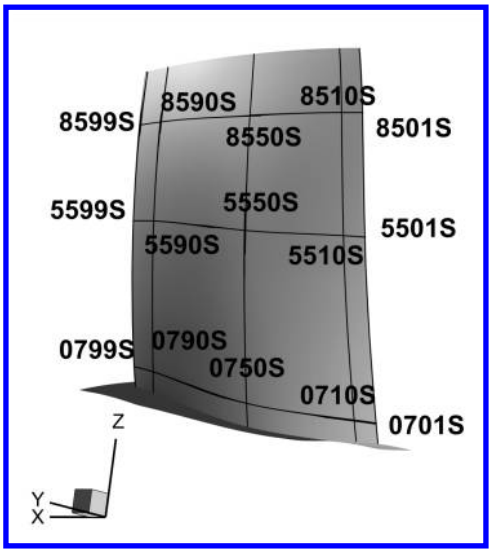

Figure 3 Numerical probes on suction surface of Rotor blade

VII. Results and Discussion

A. Campbell diagram

Fig. 4 depicts the Campbell diagram to evaluate a blade frequency. The vertical line represents the operating speed of the compressor. Its intersection with the engine order line (EOL) helps to understand a possible synchronous vibration frequency. The rig test of the compressor is shown to have a step change in the NSV frequency from 2661 to 2600 Hz which is located between 12 and 13 EOL lines. The first torsional mode natural frequency of the blade is 2621 Hz. The predicted NSV frequency is 2595 Hz, an excellent agreement with the experiment. It should be noted that this frequency is based on the frequency analysis of the suction surface rotor blade static pressure for last three rotor revolutions to avoid the transition period results as the unsteady computation is started from the steady state RANS solution obtained with a mixing plane approach between different blade rows.

B. Blade Surface Static Pressure

The instantaneous normalized static pressure for numerical probes at 10 % axial chord is shown in Fig. 5. The suction side pressure is shown on the left and the pressure side on the right. These pressure signals exhibit different

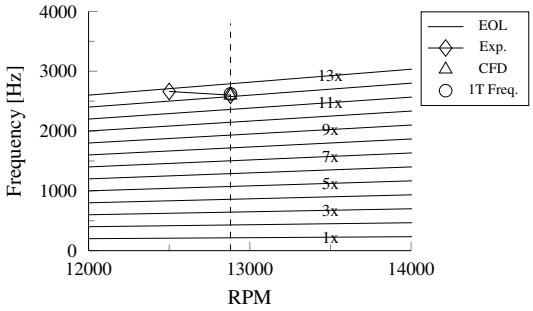

Figure 4 Campbell diagram

energy spectrum frequencies instead of one distinct frequency. The amplitude of fluctuation is more pronounce at 85 % span location as compared to other numerical probes signal and overall amplitude of fluctuation is higher on the pressure side as compared to the suction side.

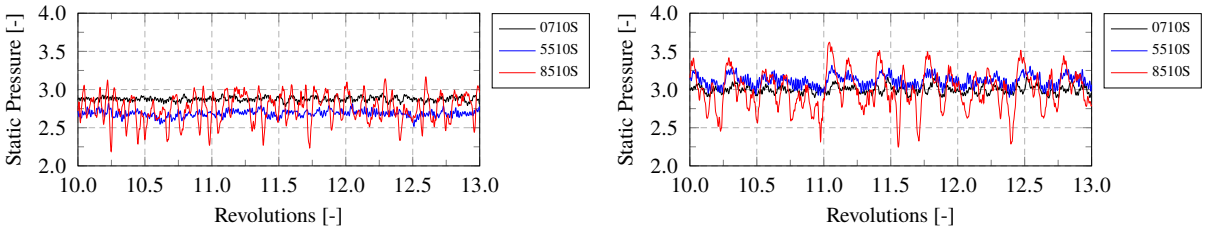

(a) Suction surface **(b) Pressure surface**

Figure 5 Instantaneous Blade-1 surface static pressure

The frequency spectrum analysis of all numerical probes on blade-1 is shown in Fig. 6. The suction surface numerical probes results are presented on the left-hand side and the pressure surface on the right-hand side. At 7 % span location, two dominant frequencies are 12,101 Hz and 2525 Hz. The first one is the IGV blade passing frequency and the other is the non-engine order vibration frequency. The IGV blade passing frequency drops sharply slightly away from the leading edge. The amplitude of this frequency is significantly higher near the leading edge at 55 % span and a drop in its magnitude similar to 7 % span is observed. The effect of this frequency at 85 % span is negligible as compared to other frequencies. The NSV frequency of 2595 Hz is present at 85 % radial span on the suction surface of rotor blade at 10 % and 50 % axial chord. On the pressure side however this frequency is not captured distinctly like on the suction side and the dominant frequency is close to the first natural frequency, i.e., 1065.5 Hz. The lower frequencies at this span location hint towards various length scale eddies due to the complex interaction of a tornado-like tip vortex, the incoming flow and the tip leakage flow. It should also be noted that Blade-3 and Blade-4 have not captured the NSV frequency close to the experimental value in the last three revolutions.

C. Structural Displacement

The mean generalized modal displacement is not zero due to the initial static loading, Fig. 7. The modal displacement of mode-1 is significantly higher than the mode-2. From the sixth revolution onwards, the modal displacement exhibits the limit cycle oscillation with a beating effect due to the vibration generated by different length scale eddies of separated flow. The non-synchronous vibration is observed close to the second mode natural frequency.

The instantaneous leading edge tip displacement of blade-1 is shown in Fig. 8(a). The frequency spectrum analysis based on this displacement is carried out for all the blades, Fig. 8(b). The amplitude of mode-1 frequency is significantly higher than the next dominant frequency, which is in line with the predicted modal displacement amplitude. Similar high content amplitude of frequency 1154 Hz is observed for the numerical probe 8501P, which is near the rotor tip leading edge on the pressure surface.

The tip displacement and the blade surface static pressure oscillation are stable. This hints at the stable operation of the compressor without a breakdown due to the traveling tip vortex instability.

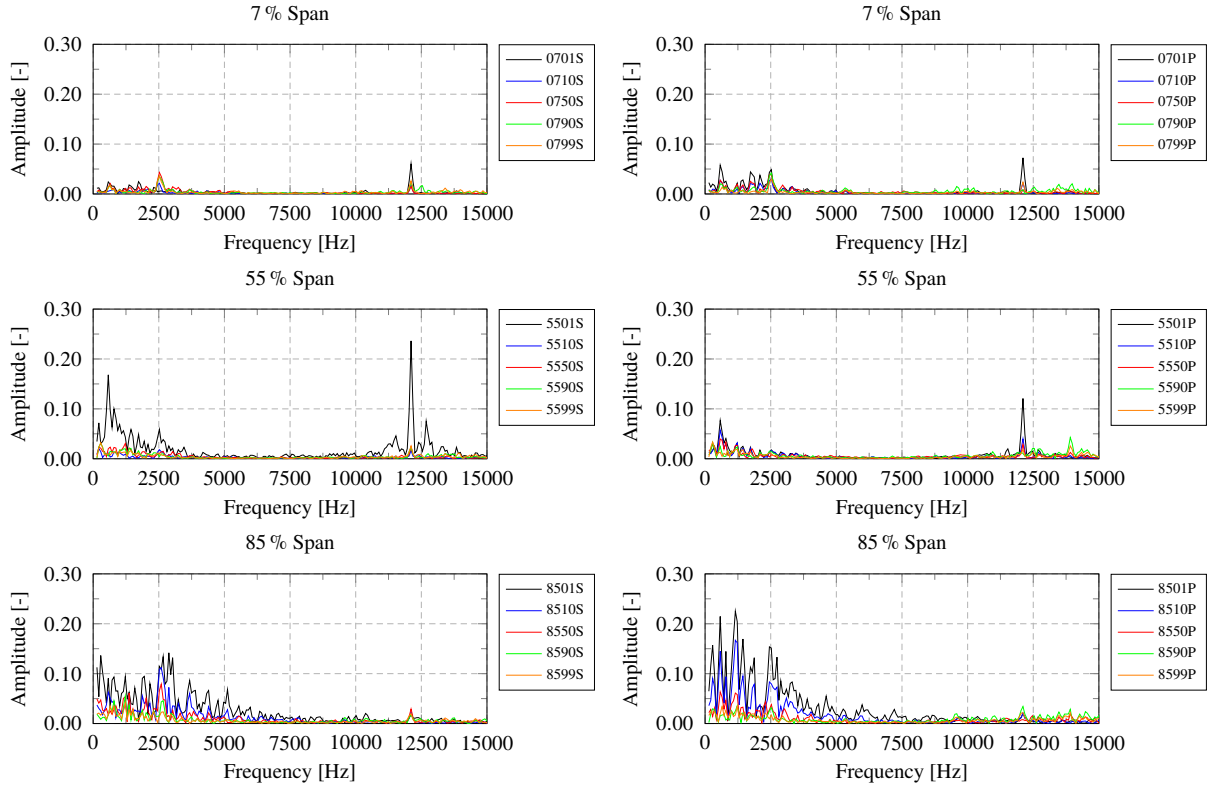

(a) Suction surface **(b) Pressure surface**

Figure 6 Frequency analysis of Blade-1 surface static pressure

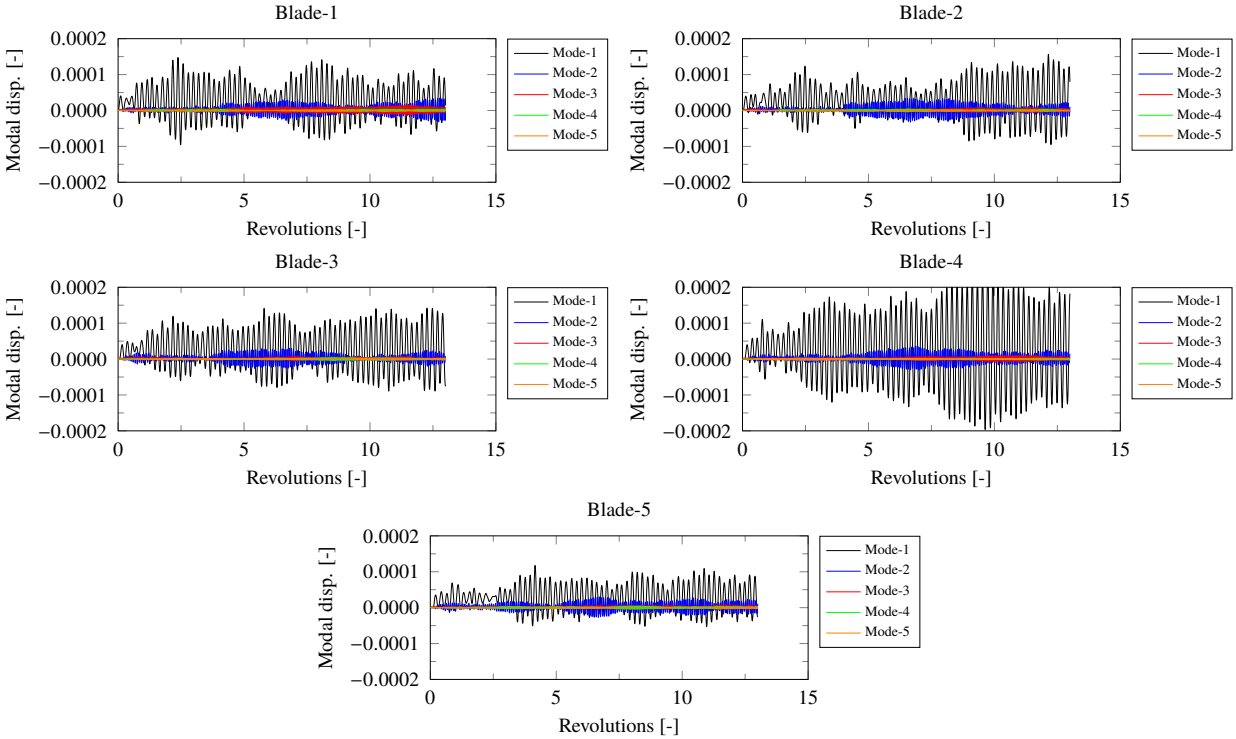

Figure 7 Generalized modal displacement of blade tip leading edge

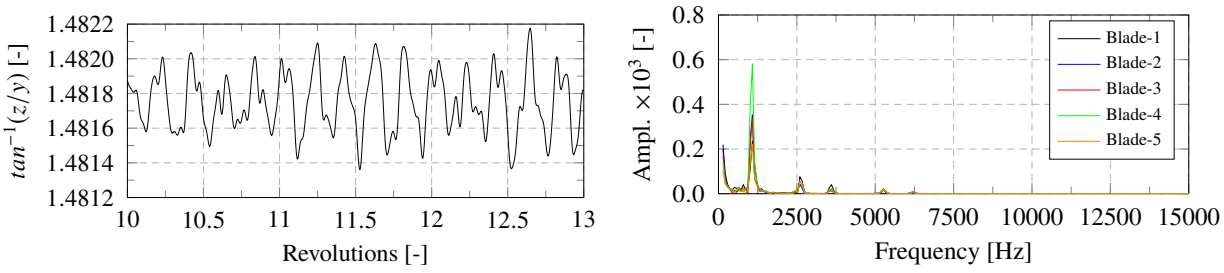

(a) Blade-1 **(b) Frequency analysis**

Figure 8 Leading edge tip displacement of rotor blades

D. Flow Structure and Instabilities

The wake propagation and vortex instabilities are fully conserved, Fig. 9, with the fully conservative sliding BC. The rotor blades cut the upstream IGV wakes and the stator blades cut the rotor wake. The flow structure near the LE of the rotor blade is different at a particular instant in time. The stator wake is unstable owing to its interaction with the rotor wake and its instability. In the Figs. 9 to 13, 0/70 to 5/70 refer the instant after twelve revolutions.

The instantaneous tip vortex streamlines near the leading edge is contoured with the normalized axial velocity, Fig. 10. A tornado-like tip vortex is residing on the blade-2 suction surface at 0/70 revolution, Fig. 10. Unlike the typical streamwise tip clearance vortex, it is traveling in the counter-rotating direction and moves to the adjacent blade leading edge at 4/70 revolution. After reaching the leading edge of the adjacent blade, it moves from the pressure side to the suction side and travels along the streamwise direction till it reaches the throat area formed by aft part of the current blade and the leading edge of the adjacent blade. The complex interaction of the incoming flow and the vortex allows it travel and stay longer on the suction of the blade. This vortex motion can be seen between blade-2 and blade-3 in Fig. 10 and it creates an oscillating blade force to induce the NSV.

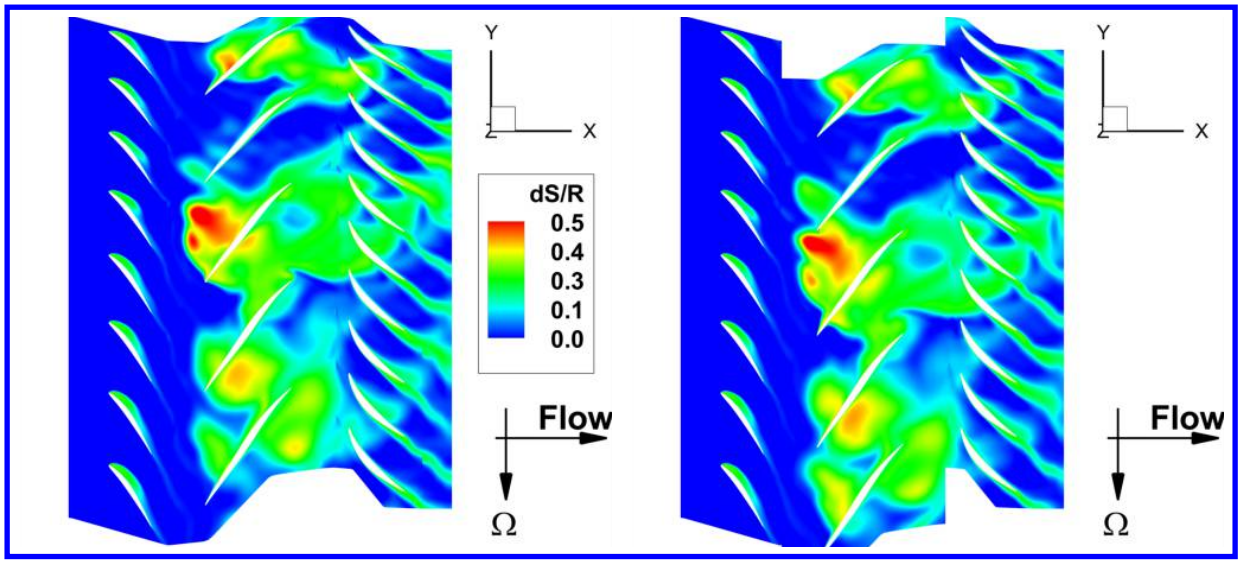

(a) 0/70 **(b)** 1/70

Figure 9 Wake propagation at 85 % span

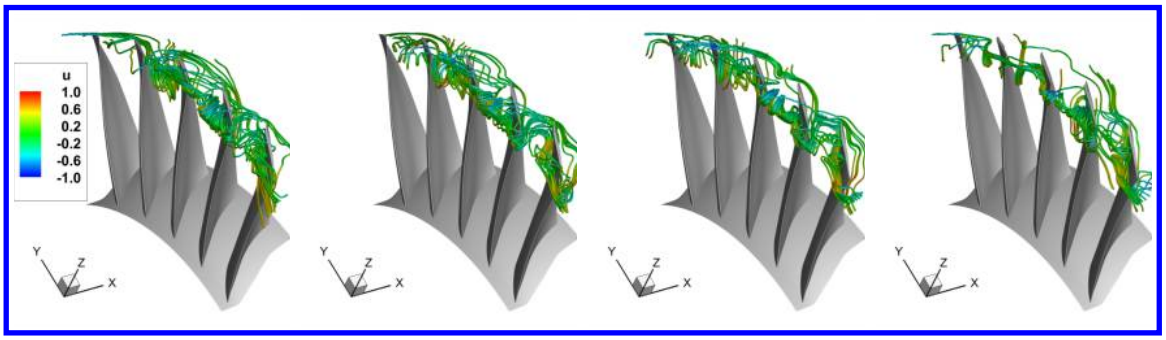

(a) 0/70 **(b)** 1/70 **(c)** 2/70 **(d)** 3/70

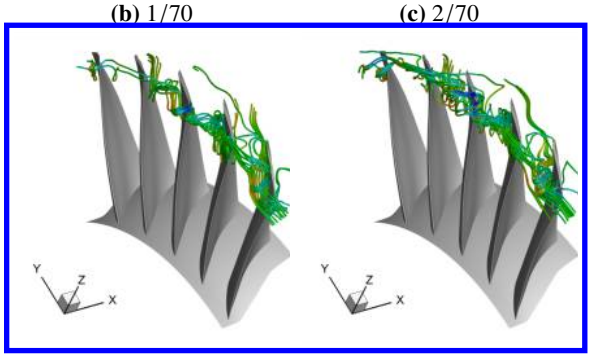

(e) 4/70 **(f)** 5/70

Figure 10 Rotor tip flow instability

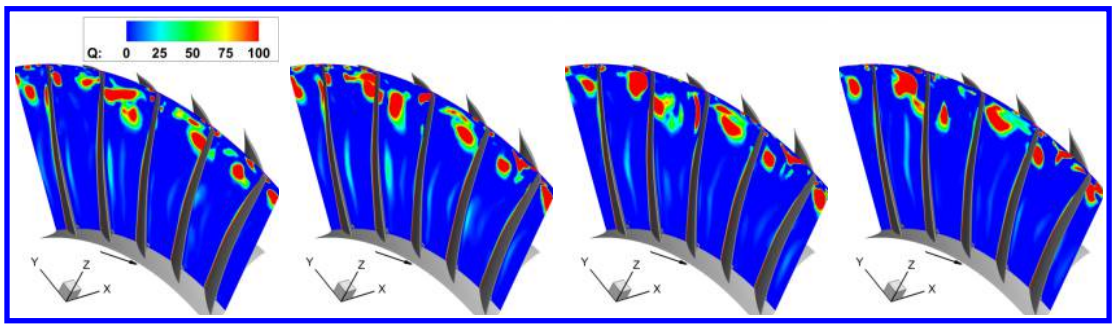

(a) 0/70 **(b)** 1/70 **(c)** 2/70 **(d)** 3/70

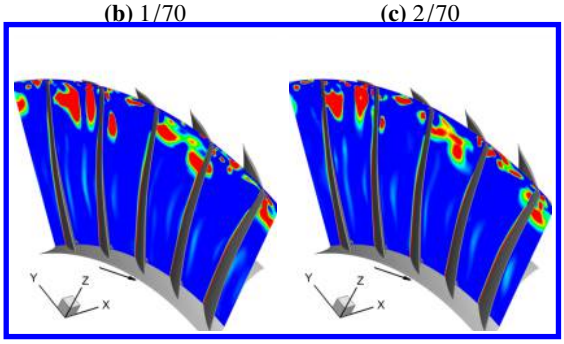

(e) 4/70 **(f)** 5/70

Figure 11 Q criterion

Fig. 11 shows the contour of Q criterion near the rotor leading edge. The vortex of different length scales is concentrated above 75 % span location due to the tornado-like vortex effect and tip flow instability. The counter-rotating direction of this vortex can be seen from the instantaneous contour plot. This also shows the region of high entropy due

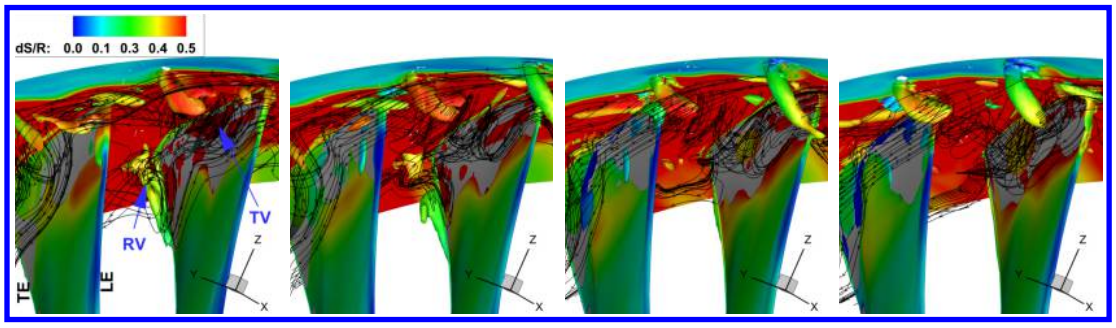

(a) 0/70 **(b)** 1/70 **(c)** 2/70 **(d)** 3/70

(e) 4/70 **(f)** 5/70

Figure 12 Iso-surfaces of $\lambda_{ci} = 15$ in the tip region of the Rotor

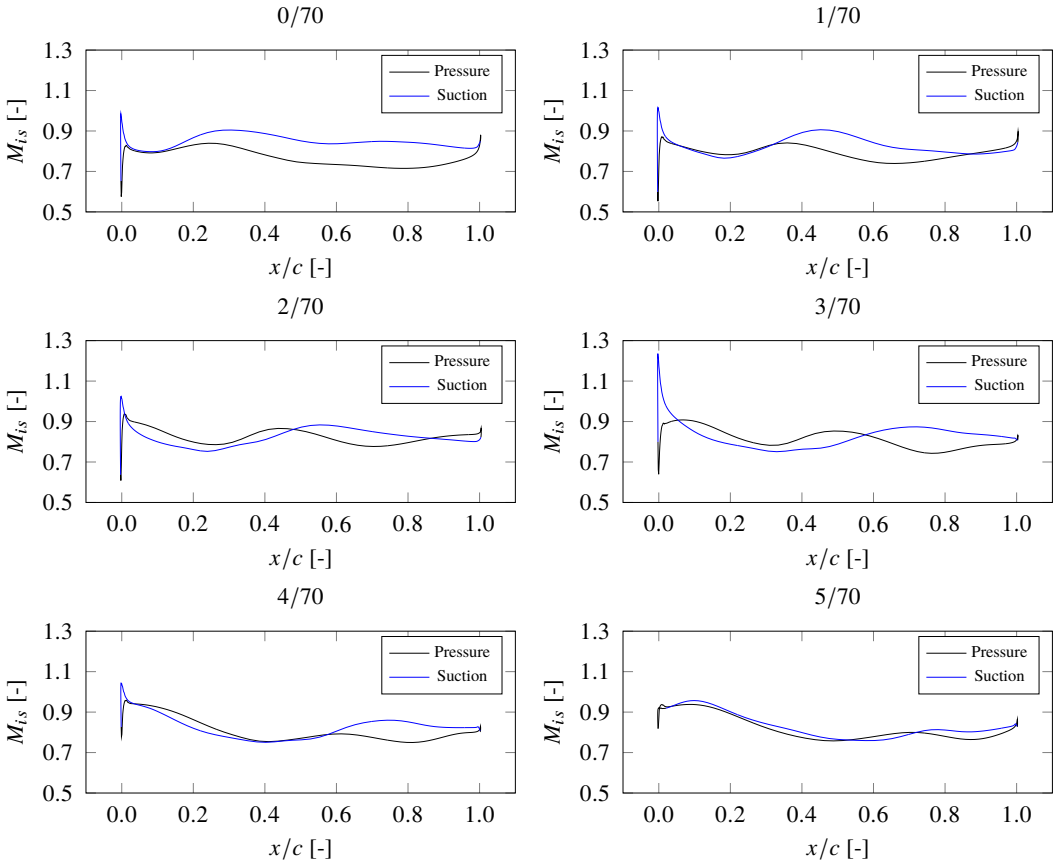

Figure 13 Blade-1 loading at 85 % span

to the interaction of incoming flow and the tip vortex.

The vortices are distinguished with the swirling strength (λ_{ci}) criterion after Zhou et al. [34]. The iso-surfaces are contoured with the entropy. Apart from the TV, Radial Vortex (RV) is also observed in the upper rotor span region and its appearance is random. Based on Brandstetter [11], these RVs cause the NSV.

E. Blade loading

Fig. 13 illustrates the blade loading at 85 % location, where the NSV is predicted in the present study. At 3/70 revolution , Fig. 10, the tip vortex is near the leading edge of blade-1. This leads to a high incidence angle and blade loading near the leading edge. Its motion along the suction surface causes the localized blade loading oscillation and promotes the non-synchronous vibration. Due to the high blockage generated by the traveling vortices, the blade loading is overall very low.

VIII. Conclusions

The non-synchronous vibration of a 1-1/2 stage high-speed axial compressor is investigated with the fully coupled fluid-structure interaction. A high-fidelity simulation is carried out using the DDES turbulence model with the fully conservative sliding BC between the blade rows. A 1/7th annulus section is used with the time-shifted phase lag BC at circumferential boundaries to reduce computational efforts.

The compressor is operating within the stability margin without breakdown due to the traveling tip vortex instability. A tornado-like tip vortex originated near the leading edge of the rotor travels in the streamwise direction along the suction surface a blade before moving to the adjacent blade leading edge in the counter-rotating direction. This vortex motion causes the unsteady blade loading and induces the non-engine order vibration near the first torsional mode. In the rotor tip region, RV appears randomly. The predicted NSV frequency of 2595 Hz shows an excellent agreement with the rig test measured frequency of 2600 Hz.

Acknowledgments

We would like to thank the Center for Computational Science at the University of Miami, Coral Gables for providing computational resources. We thank GE for approval of publishing the NSV research under the GUIde 4 program.

References

[1] Cumpsty, N. A., *Compressor Aerodynamics*, 2nd ed., Krieger Publishing Company, 2004.

[2] Kielb, R. E., Barter, J. W., Thomas, J. P., and Hall, K. C., "Blade Excitation by Aerodynamic Instabilities: A Compressor Blade Study," 2003, pp. 399–406. doi:10.1115/gt2003-38634, URL http://dx.doi.org/10.1115/GT2003-38634, GT2003-38634.

[3] Baumgartner, M., Kameier, F., and Hourmouziadis, J., "Non-Engine Order Blade Vibration in a High Pressure Compressor," *Twelfth International Symposium on Airbreathing Engines*, Melbourne, Australia, 1995. URL https://hal.archives-ouvertes.fr/hal-01353829.

[4] Mailach, R., Lehmann, I., and Vogeler, K., "Rotating Instabilities in an Axial Compressor Originating From the Fluctuating Blade Tip Vortex," *Journal of Turbomachinery*, Vol. 123, No. 3, 2001.

[5] März, J., Hah, C., and Neise, W., "An Experimental and Numerical Investigation into the Mechanisms of Rotating Instability," *Journal of Turbomachinery*, Vol. 124, No. 3, 2002, pp. 367–374.

[6] Thomassin, J., Vo, H. D., and Mureithi, N. W., "The tip clearance flow resonance behind axial compressor nonsynchronous vibration," *Journal of Turbomachinery*, Vol. 133, No. 4, 2011.

[7] Drolet, M., Vo, H. D., and Mureithi, N. W., "Effect of Tip Clearance on the Prediction of Nonsynchronous Vibrations in Axial Compressors," *Journal of Turbomachinery*, Vol. 135, No. 1, 2013.

[8] Im, H., and Zha, G., "Investigation of Flow Instability Mechanism Causing Compressor Rotor-Blade Nonsynchronous Vibration," *AIAA Journal*, Vol. 52, No. 9, 2014, pp. 2019–2031. doi:10.2514/1.J052781, URL https://doi.org/10.2514/1.J052781.

[9] Im, H., and Zha, G., "Investigation of Non-synchronous Vibration Mechanism for a High Speed Axial Compressor Using Delayed DES," AIAA SciTech Forum, American Institute of Aeronautics and Astronautics, 2014. doi:10.2514/6.2014-0789, URL https://doi.org/10.2514/6.2014-0789.

[10] Thomassin, J., Vo, H. D., and Mureithi, N. W., "Blade tip clearance flow and compressor nonsynchronous vibrations: the jet core feedback theory as the coupling mechanism," *Journal of Turbomachinery*, Vol. 131, No. 1, 2009.

[11] Brandstetter, C., Jüngst, M., and Schiffer, H.-P., "Measurements of Radial Vortices, Spill Forward, and Vortex Breakdown in a Transonic Compressor," *Journal of Turbomachinery*, Vol. 140, No. 6, 2018. doi:10.1115/1.4039053, URL https://doi.org/10.1115/1.4039053, TURBO-17-1218.

[12] Spalart, P. R., Jou, W.-H., Strelets, M., and Allmaras, S., "Comments on the Feasibility of LES for Wings, and on a Hybrid RANS/LES Approach," 1997.

[13] Spalart, P. R., and Squires, K. D., "The Status of Detached-Eddy Simulation for Bluff Bodies," *The Aerodynamics of Heavy Vehicles: Trucks, Buses, and Trains*, edited by R. McCallen, F. Browand, and J. Ross, Springer Berlin Heidelberg, Berlin, Heidelberg, 2004, pp. 29–45.

[14] Spalart, P. R., "Detached-Eddy Simulation," *Annual Review of Fluid Mechanics*, Vol. 41, No. 1, 2009, pp. 181–202. doi:10.1146/annurev.fluid.010908.165130, URL https://doi.org/10.1146/annurev.fluid.010908.165130.

[15] Spalart, P. R., Deck, S., Shur, M. L., Squires, K. D., Strelets, M. K., and Travin, A. K., "A New Version of Detached-eddy Simulation, Resistant to Ambiguous Grid Densities," *Theoretical and Computational Fluid Dynamics*, Vol. 20, No. 3, 2006, p. 181. doi:10.1007/s00162-006-0015-0, URL https://doi.org/10.1007/s00162-006-0015-0.

[16] Menter, F. R., and Kuntz, M., "Adaptation of Eddy-Viscosity Turbulence Models to Unsteady Separated Flow Behind Vehicles," *The Aerodynamics of Heavy Vehicles: Trucks, Buses, and Trains*, edited by R. McCallen, F. Browand, and J. Ross, Springer Berlin Heidelberg, Berlin, Heidelberg, 2004, pp. 339–352.

[17] Sanders, A., "Nonsynchronous vibration (NSV) due to a flow-induced aerodynamic instability in a composite fan stator.(Author Abstract)," *Journal of Turbomachinery*, Vol. 127, No. 2, 2005.

[18] Clark, S. T., Besem, F. M., Kielb, R. E., and Thomas, J. P., "Developing a Reduced-Order Model of Nonsynchronous Vibration in Turbomachinery Using Proper-Orthogonal Decomposition Methods," *Journal of Engineering for Gas Turbines and Power*, Vol. 137, No. 5, 2015. doi:10.1115/1.4028675, URL https://doi.org/10.1115/1.4028675, 052501.

[19] Espinal, D., Im, H.-S., and Zha, G.-C., "Full-Annulus Simulation of Nonsynchronous Blade Vibration Excitation of an Axial Compressor," *Journal of Turbomachinery*, Vol. 140, No. 3, 2017. doi:10.1115/1.4038337, URL https://doi.org/10.1115/1.4038337, 031008.

[20] Fiquet, A.-L., Brandstetter, C., Aubert, S., and Philit, M., "Non-engine order oscillations in an axial multi-stage compressor - aeroacoustic Interaction," 2018. ISUAAAT15-087.

[21] Drolet, M., Thomassin, J., Vo, H., and Mureithi, N., "Numerical Investigation Into Non-Synchronous Vibrations of Axial Flow Compressors by the Resonant Tip Clearance Flow," 2009. doi:10.1115/GT2009-59074.

[22] Patel, P., Im, H.-S., and Zha, G., *Numerical investigation of Non-Synchronous vibration using Scale Adaptive Simulation turbulence model*, 2019. doi:10.2514/6.2019-4175, URL https://arc.aiaa.org/doi/abs/10.2514/6.2019-4175.

[23] Im, H.-S., and Zha, G.-C., "Effects of Rotor Tip Clearance on Tip Clearance Flow Potentially Leading to NSV in an Axial Compressor," 2012, pp. 1383–1394. URL http://dx.doi.org/10.1115/GT2012-68148, GT2012-68148.

[24] Allmaras, S., Johnson, F., and Spalart, P., "Modifications and Clarifications for the Implementation of the Spalart-Allmaras Turbulence Model," Seventh International Conference on Computational Fluid Dynamics (ICCFD7), 2012.

[25] Patel, P., and Zha, G., "Investigation of mixed Micro-Compressor casing treatment using non-matching mesh interface," 2019. GT2019-90977.

[26] Jameson, A., "Time dependent calculations using multigrid, with applications to unsteady flows past airfoils and wings," Fluid Dynamics and Co-located Conferences, American Institute of Aeronautics and Astronautics, 1991. doi:10.2514/6.1991-1596, URL https://doi.org/10.2514/6.1991-1596.

[27] Srinivasan, A. V., "Flutter and Resonant Vibration Characteristics of Engine Blades," *Journal of Engineering for Gas Turbines and Power*, Vol. 119, No. 4, 1997, pp. 742–775. doi:10.1115/1.2817053, URL http://dx.doi.org/10.1115/1.2817053.

[28] Chen, X., Zha, G.-C., and Yang, M.-T., "Numerical simulation of 3-D wing flutter with fully coupled fluid–structural interaction," *Computers & Fluids*, Vol. 36, No. 5, 2007, pp. 856 – 867. doi:https://doi.org/10.1016/j.compfluid.2006.08.005, URL http://www.sciencedirect.com/science/article/pii/S0045793006001034.

[29] Im, H.-S., and Zha, G.-C., "Simulation of Non-Synchronous Blade Vibration of an Axial Compressor Using a Fully Coupled Fluid/Structure Interaction," 2012, pp. 1395–1407. doi:10.1115/gt2012-68150, URL http://dx.doi.org/10.1115/GT2012-68150, GT2012-68150.

[30] Im, H., Chen, X., and Zha, G., "Detached Eddy Simulation of Unsteady Stall Flows of a Full Annulus Transonic Rotor," *Journal of Propulsion and Power*, Vol. 28, No. 4, 2011. doi:10.2514/1.B34395.

[31] Im, H., Chen, X., and Zha, G., "Simulation of 3D Multistage Axial Compressor Using a Fully Conservative Sliding Boundary Condition," 2011, pp. 1321–1330. doi:10.1115/imece2011-62049, URL http://dx.doi.org/10.1115/IMECE2011-62049, IMECE2011-62049.

[32] Wang, B., Hu, Z., and Zha, G., "A General Sub-Domain Boundary Mapping Procedure For Structured Grid CFD Parallel Computation," *AIAA Journal of Aerospace Computing, Information, and Communication*, Vol. 5, 2008, pp. 425–447.

[33] Im, H., Chen, X., and Zha, G., "Detached Eddy Simulation of Transonic Rotor Stall Flutter Using a Fully Coupled Fluid-Structure Interaction," 2011. doi:10.1115/GT2011-45437.

[34] Zhou, J., Adrian, R., Balachandar, S., and Kendall, T., "Mechanisms for generating coherent packets of hairpin vortices in channel flow," *Journal of Fluid Mechanics*, Vol. 387, 1999, pp. 353–396. doi:10.1017/S002211209900467X.